Geochemistry Geophysics Geosystems G3
AN ELECTRONIC JOURNAL OF THE EARTH SCIENCES
Published by AGU and the Geochemical Society

Article
Volume 8, Number 8
9 August 2007
Q08004, doi:10.1029/2007GC001629
ISSN: 1525-2027

Crustal structure of the Trans-Atlantic Geotraverse (TAG) segment (Mid-Atlantic Ridge, 26°10′N): Implications for the nature of hydrothermal circulation and detachment faulting at slow spreading ridges

J. Pablo Canales and Robert A. Sohn
Woods Hole Oceanographic Institution, MS 24, 360 Woods Hole Road, Woods Hole, Massachusetts 02543, USA (jpcanales@whoi.edu)

Brian J. deMartin
Department of Geological Sciences, Brown University, Providence, Rhode Island 02912, USA

[1] New seismic refraction data reveal that hydrothermal circulation at the Trans-Atlantic Geotraverse (TAG) hydrothermal field on the Mid-Atlantic Ridge at 26°10′N is not driven by energy extracted from shallow or mid-crustal magmatic intrusions. Our results show that the TAG hydrothermal field is underlain by rocks with high seismic velocities typical of lower crustal gabbros and partially serpentinized peridotites at depth as shallow as 1 km, and we find no evidence for low seismic velocities associated with mid-crustal magma chambers. Our tomographic images support the hypothesis of Tivey et al. (2003) that the TAG field is located on the hanging wall of a detachment fault, and constrain the complex, dome-shaped subsurface geometry of the fault system. Modeling of our seismic velocity profiles indicates that the porosity of the detachment footwall increases after rotation during exhumation, which may enhance footwall cooling. However, heat extracted from the footwall is insufficient for sustaining long-term, high-temperature, hydrothermal circulation at TAG. These constraints indicate that the primary heat source for the TAG hydrothermal system must be a deep magma reservoir at or below the base of the crust.

Components: 8949 words, 13 figures, 1 table.

Keywords: TAG hydrothermal field; crustal structure; detachment faulting; Mid-Atlantic Ridge; slow spreading ridge.

Index Terms: 7220 Seismology: Oceanic crust; 7245 Seismology: Mid-ocean ridges; 8135 Tectonophysics: Hydrothermal systems (0450, 1034, 3017, 3616, 4832, 8424).

Received 20 March 2007; **Revised** 6 June 2007; **Accepted** 19 June 2007; **Published** 9 August 2007.

Canales, J. P., R. A. Sohn, and B. J. deMartin (2007), Crustal structure of the Trans-Atlantic Geotraverse (TAG) segment (Mid-Atlantic Ridge, 26°10′N): Implications for the nature of hydrothermal circulation and detachment faulting at slow spreading ridges, *Geochem. Geophys. Geosyst.*, *8*, Q08004, doi:10.1029/2007GC001629.

1. Introduction

[2] High-temperature hydrothermal circulation on mid-ocean ridges plays an important role in the exchange of heat and mass between the Earth's lithosphere and oceans. It has been proposed that hydrothermal convection may be driven by either heat extracted from a crystallizing magma reservoir [e.g., *Cann et al.*, 1985], or by cracking fronts propagating through hot but solid rock [e.g., *Lister*,

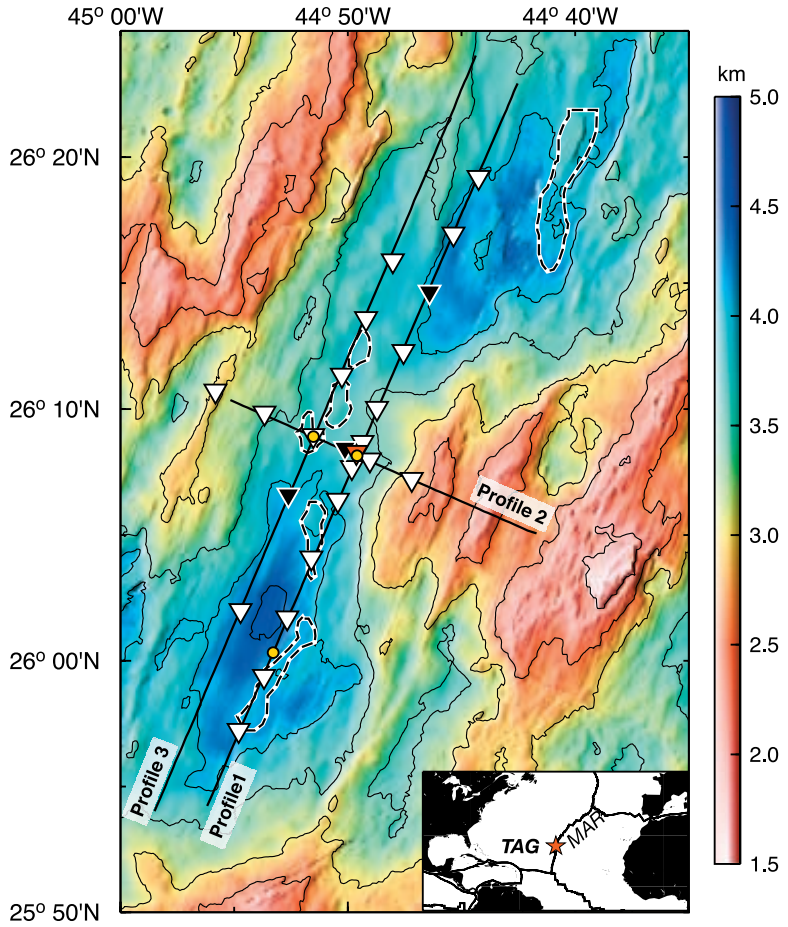

Figure 1. Bathymetry of the TAG segment and seismic profiles presented in this study. Triangles are OBS. Red triangle also indicates the location of the TAG hydrothermal mound. Black triangles correspond to the OBS whose data are shown in Figure 2. Yellow circles show the location of the velocity-depth profiles shown in Figure 7. Dashed lines outline neovolcanic zones [*Tivey et al.*, 2003]. Inset shows the location of the TAG segment along the MAR.

1974]. *Wilcock and Delaney* [1996] have further proposed that the dominant mechanism of heat extraction depends on geological factors related to spreading rate, with circulation at fast spreading ridges, such as the East Pacific Rise (EPR), extracting heat from a shallow crustal magma chamber, while circulation at slower spreading ridges, such as the Mid-Atlantic Ridge (MAR), utilizes deeply penetrating faults to extract heat from a broad cracking front.

[3] However, *Cann and Strens* [1982] argue that cracking fronts are not capable of providing high-temperature fluids over geologically significant timescales, and all of the seismic studies conducted to date in the vicinity of known high-temperature hydrothermal systems have detected the presence of crustal melt, irrespective of spreading rate. Seismic reflections from crustal melt lenses have been observed beneath high-temperature hydrothermal systems at the southern [e.g., *Singh et al.*, 1998] and northern EPR [e.g., *Detrick et al.*, 1987], the intermediate-spreading Juan de Fuca Ridge [e.g., *Canales et al.*, 2006; *Van Ark et al.*, 2007], the back-arc Eastern Lau Spreading Center [e.g., *Martinez et al.*, 2006], and the MAR near 37°40′N [*Singh et al.*, 2006]. Tomographic images of low seismic velocities indicative of crustal partial melt have also been obtained near high-temperature hydrothermal systems at the northern EPR [*Dunn et al.*, 2000] and the MAR near 23°20′N [*Canales et al.*, 2000]. These results challenge the cracking front model, and suggest that high-temperature hydrothermal fields are associated with heat extraction from crustal melt reservoirs regardless of spreading rate and geological setting. A possible exception to this rule is the Trans-Atlantic Geotraverse (TAG) hydrothermal field on the MAR at 26°10′N (full spreading rate of 21 mm yr^{-1} [*Tivey et al.*, 2003]; Figure 1),

where anomalously low seismic velocities reported in an early seismic study [*Kong et al.*, 1992] have been interpreted in different ways by several authors: as hot but solid rock in support of the cracking front hypothesis [e.g., *Wilcock and Delaney*, 1996], as well as crustal melt reservoirs in support of the crystallizing magma chamber hypothesis [e.g., *Humphris and Cann*, 2000].

[4] The TAG hydrothermal field is composed of a low-temperature alteration zone, five inactive, high-temperature hydrothermal deposits, and the active TAG mound, which is the largest high-temperature hydrothermal deposit found to date on the seafloor [e.g., *Rona et al.*, 1986]. The mineralogy and structure of the active TAG mound and the tectonic context of the TAG field have been extensively studied [e.g., *Humphris et al.*, 1995; *Kleinrock and Humphris*, 1996; *Lalou et al.*, 1995; *Zonenshain et al.*, 1989]. High-temperature discharge has been occurring on a fissured zone of the rift valley floor near the eastern valley wall [e.g., *Kleinrock and Humphris*, 1996] for the past ~150 kyr, which has generated ~3.9 million tonnes of massive sulfide deposits [*Humphris et al.*, 1995].

[5] The anomalously low seismic velocities reported by *Kong et al.* [1992], combined with the observation of a neovolcanic zone in the axial valley east of the hydrothermal field [e.g., *Kleinrock and Humphris*, 1996], has, until recently, led most researchers to believe that mid-crustal magma injections are the primary heat source driving hydrothermal convection beneath TAG. However, other studies have shown that faulting and tectonic extension play an important role in this system. Gabbro exposures have been observed along a fault scarp to the east of the TAG mound [*Zonenshain et al.*, 1989], suggesting uplift of intrusive crustal rocks along the eastern valley wall. In addition, near-bottom magnetic data have shown that the eastern valley wall is characterized by a low-magnetization anomaly that is best explained by crustal thinning from extension along a detachment fault [*Tivey et al.*, 2003]. Modeling of the magnetic data suggests that the fault has been active since ~0.35 Ma, and has accommodated about 4 km of horizontal extension [*Tivey et al.*, 2003]. These results suggest that the active TAG mound is located on the hanging wall of a detachment fault, about 2.5 km away from the fault termination.

[6] In this paper we present results from a controlled-source seismic tomography experiment carried out to characterize the crustal structure of the TAG segment and constrain the nature and position of the heat source driving high-temperature hydrothermal circulation. Our results do not agree with the previously reported seismic structure of the TAG segment by *Kong et al.* [1992]. We find that the seismic structure beneath the active TAG mound is remarkably different from the seismic structure beneath other high-temperature hydrothermal systems [*Canales et al.*, 2000; *Dunn et al.*, 2000], and is inconsistent with the existence of upper or mid-crustal melt reservoirs large enough to drive convection at the TAG system. Instead, seismic velocities beneath the hydrothermal field are typical of lower crustal and upper mantle rocks, with a subsurface geometry that is consistent with exhumation on a dome-shaped detachment fault. When all of the geological and geophysical evidence is taken together we find that the heat source driving the TAG system must be located at or below the crust-mantle boundary.

2. Data and Method

[7] We conducted a controlled-source seismic refraction experiment along three profiles at the TAG segment during October–November 2003 (Figure 1). We used the R/V *Maurice Ewing*'s 20-unit tuned air-gun array with a total volume of 8760 cubic inch (143.6 L) to trigger seismic sources every 350 m along the profiles. Body waves from the towed source were recorded by two sets of ocean bottom seismometers (OBS). One set of 15 OBS, with a sampling rate of 125 Hz, was deployed along the profiles at ~4.5 km intervals. A second set of 9 OBS, with a sampling rate of 100 Hz, was centered on the active TAG mound for a microseismicity study [*deMartin et al.*, 2007], but the instruments were deployed on the seismic profiles to improve the spatial resolution of our survey in the immediate vicinity of the TAG hydrothermal field.

[8] Profile 1 was located along the eastern side of the rift valley floor, over the fissured area referred to as zone 3 by *Kleinrock and Humphris* [1996], and passed directly over the active TAG mound (Figure 1). This profile runs very close to a volcanic feature at 26°06′N that *Kong et al.* [1992] argued is the site of recent crustal magma injection. Profile 3 was located ~3.5 km west of, and parallel to, Profile 1, and passed over young volcanic terrain referred to as zone 2 by *Kleinrock and Humphris* [1996]. Profile 2 ran across the axial valley orthogonal to the other profiles, and crossed Profile 1 at the active TAG mound.

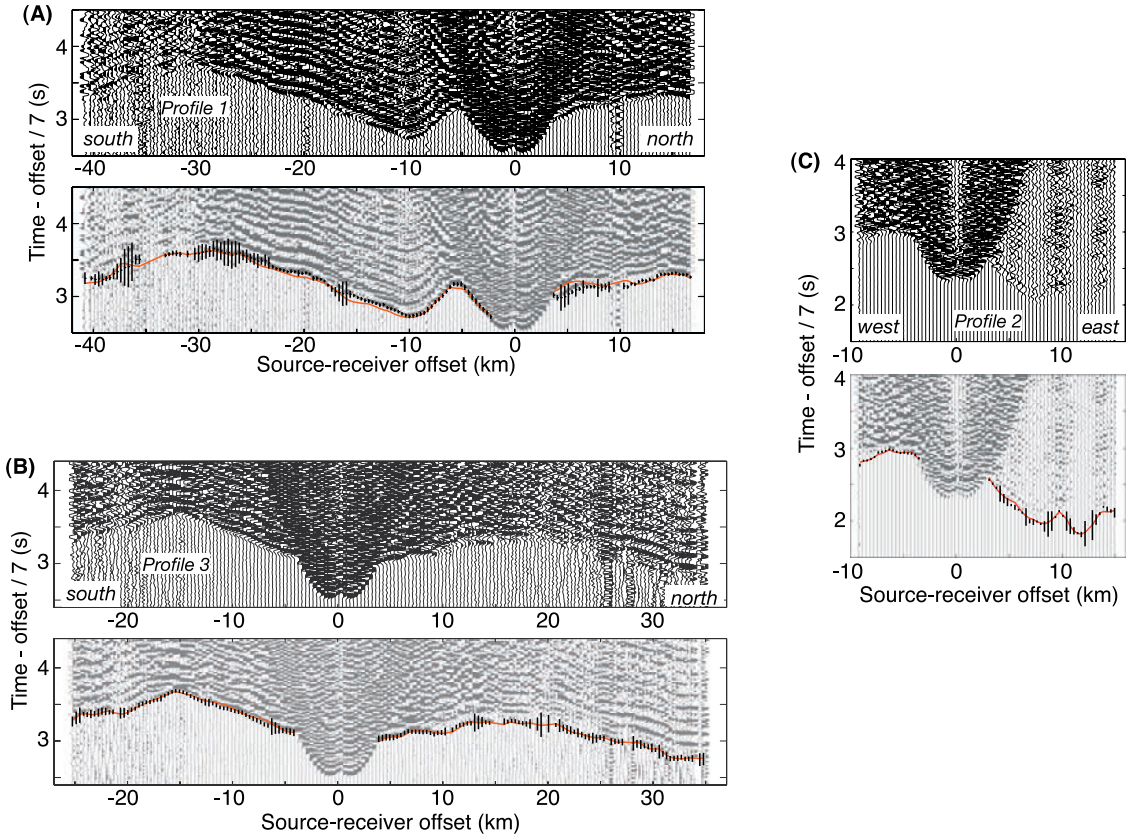

Figure 2. (a) Example seismic record section from Profile 1. Data have been band-pass filtered between 5 and 20 Hz, and amplitudes have been scaled according to range for display purposes. Bottom panel shows observed traveltime picks (vertical bars with length equal to twice the assigned uncertainty) and traveltimes predicted by the preferred 2-D model shown in Figure 6 (red line). (b and c) Same for representative record sections from Profiles 3 and 2, respectively. Locations of the instruments are shown in Figure 1 as black triangles.

[9] Maximum source-receiver offsets were 50 km, and high signal-to-noise ratio (SNR) body wave arrivals were observed at offsets of up to ~40 km (Figure 2). We used the traveltime inversion method of *Korenaga et al.* [2000] to estimate the two-dimensional (2-D) *P* wave velocity field along each profile. First arrival traveltimes were hand-picked without differentiating between crustal (P_g) or mantle (P_n) refracted phases. Traveltime uncertainties (Figure 2) were estimated incorporating effects from the SNR of the arrival [e.g., *Zelt and Forsyth*, 1994], the uncertainty of the source and receiver locations, and the uncertainty in seafloor ray entry points due to out-of-plane topography and propagation.

[10] The models were parameterized as sheared meshes hanging from the seafloor topography with 250-m lateral nodal spacing and variable vertical nodal spacing (100 m within the upper 2 km, 200 m between 2–4 km depth, and 300 m at depths >4 km). Horizontal and vertical correlation lengths (l_H and l_V, respectively) were used to impose smoothing constraints, damped by a smoothing weight λ_V to control the relative importance of the smoothing constraints with respect to the data resolution [*Korenaga et al.*, 2000]. We selected the most appropriate values of l_H, l_V, and λ_V by repeating the inversion using many combinations of these parameters, and inspecting the weighted (χ^2) residuals (Figure 3). For consistency, and for inter-comparability between inversions, we show solutions using the same set of parameters for all three of the profiles. We rejected solutions with $\chi^2 < 1$ because they over-fit the data, and found that the parameter set (l_H = 800 m, l_V = 300 m, λ_V = 100) provides the best combination for all three of the profiles.

3. Seismic Tomography Results

[11] We began our analysis by using the one-dimensional (1-D) average velocity model for the

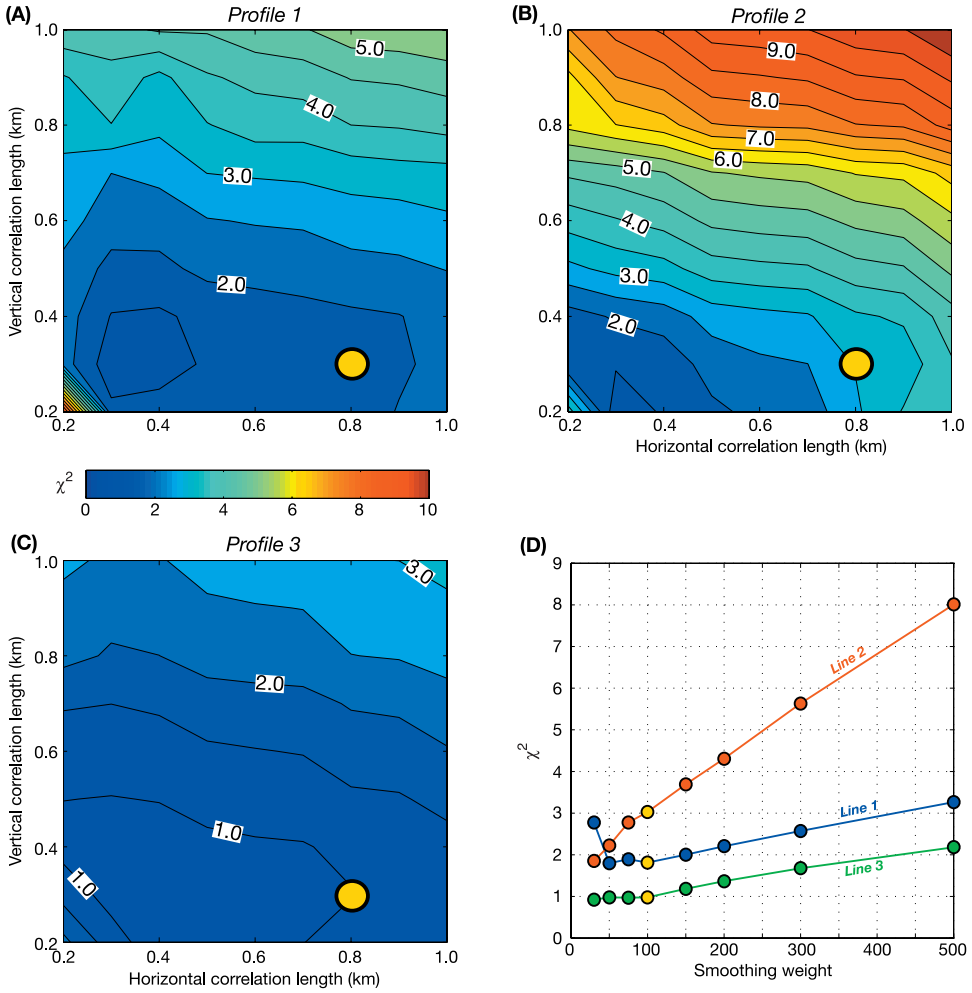

Figure 3. (a–c) Contour plots (0.5 intervals) of the traveltime misfit function χ^2 as a function of the horizontal and vertical correlation lengths for the three profiles (smoothing weight is constant at 100 in these plots). (d) Variations in χ^2 as a function of smoothing weight factor with constant horizontal and vertical correlation lengths of 800 and 300 m, respectively. Yellow circles in all panels correspond to the parameters used in the preferred inversions shown in Figure 6 (see text for details).

center of segment OH-1 near 35°N [*Hooft et al.*, 2000], hereinafter referred to as model OH-1, as our starting model (Figure 4). Forward modeling of our data using model OH-1 results in poor traveltime fits ($\chi^2 > 17$; Table 1). Traveltime residuals are biased toward negative values along Profiles 1 and 2 (Figure 5), indicating that seismic velocities along these profiles are, on average, higher than at segment OH-1. In contrast, traveltime residuals are positively biased along Profile 3 (Figure 5), indicating strong lateral variability across the rift valley floor of the TAG segment. We used model OH-1 as a starting model to invert for the best-fitting, laterally invariant 1-D structure along the three profiles (Figure 4). The 1-D inversions improve the traveltime residual statistics by reducing the variance by 7%, 18%, and 30% for Profiles 1, 2, and 3, respectively (Figure 5), but the fits are still poor ($\chi^2 > 13$; Table 1). These results demonstrate that the seismic structure of the TAG segment is not consistent with a simple 1-D model.

[12] We performed 2-D inversions of our data using the best-fitting 1-D solutions for each profile as starting models. The resulting 2-D models (Figure 6) considerably improve the traveltime fits, yielding a variance reduction of 92%, 91%, and 86% for Profiles 1, 2, and 3, respectively (Figure 5), and $\chi^2 \leq 3$ (Table 1). Predicted versus observed traveltimes for representative instruments along each of the profiles are shown in Figure 2. The velocity structure along Profile 1 is characterized by a ~20-km-long high-velocity (>6.5 km s^{-1})

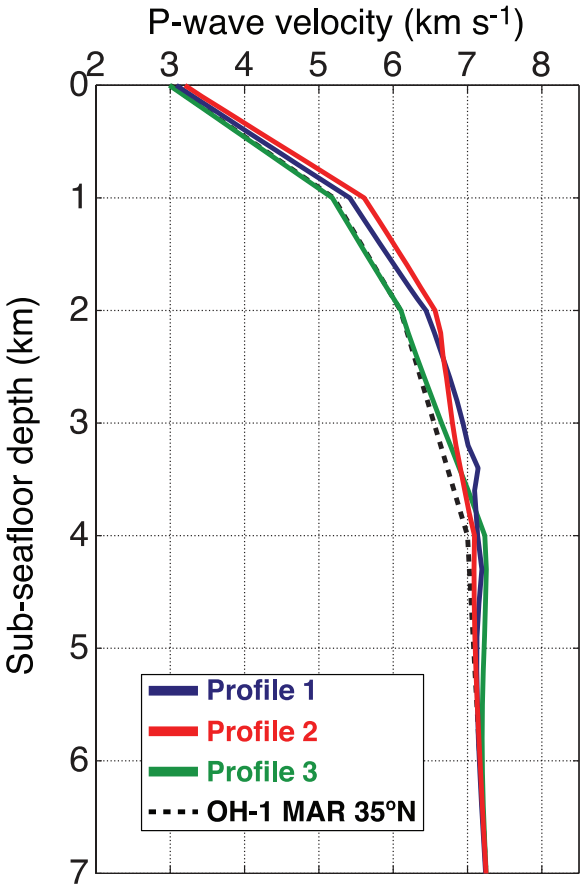

Figure 4. Best-fitting 1-D velocity versus depth profiles for each seismic profile and starting model OH-1 from the MAR near 35°N [*Hooft et al.*, 2000]. These 1-D models were used as starting velocity models for the 2-D inversions shown in Figure 6.

region with a triangular cross-section profile centered beneath the shallowest part of the seafloor near the segment center (3.75 km to the north of the active TAG mound). Within this region, velocities as high as 6.7 km s^{-1} are found at 1 km depth, and extend down to at least 5 km depth with very low velocity gradient. This high-velocity region also underlies the volcano near 26°06′N where *Kong et al.* [1992] reported anomalously low seismic velocities. Seismic velocities are also somewhat higher near the northern end of the profile, where mantle velocities (>7.5 km s^{-1}) are found at 4 km depth, compared to the southern end of the profile, where velocities increase from ~3 km s^{-1} at the seafloor to 6 km s^{-1} at 3 km depth.

[13] The velocity model along Profile 3 does not show significant lateral variations in seismic structure (Figure 6). This contrasts with the large variations found along Profile 1, despite the fact that the profiles are only ~3.5 km apart (Figure 1), indicating strong variability in axial valley crustal structure in the spreading direction. This variability is evident in the velocity model of Profile 2 (previously reported by *deMartin et al.* [2007]), which shows a highly asymmetric structure. High velocities characterize the eastern valley wall, while the valley floor and western wall display lower crustal velocities (Figure 6).

4. Interpretation and Discussion

[14] To assist in the interpretation of the velocity models, we compare 1-D velocity profiles from three locations at the TAG segment (shown in Figure 1 and Figure 6) with 1-D velocity models from other segments of the MAR (Figure 7). Seismic velocities in the upper 0.5–1.5 km beneath the active TAG mound are significantly higher than average MAR values, but below 1.5 km depth the velocities are very similar. In contrast, the velocity structure 3.5 km west of the mound is indistinguishable from MAR average values. Velocities beneath the TAG mound decrease slightly from 6.9 km s^{-1} at 2 km depth to 6.4 km s^{-1} at 2.4 km depth in our best-fit 2-D model for Profile 1 (Figure 7). Resolution tests demonstrate that this negative velocity gradient is required by the data, although there is a trade-off between the thickness and amplitude of the negative gradient region (see Appendix A). Shallow crustal velocities in the southern nodal basin at depths from 1.5–3.0 km are 1.5 km s^{-1} lower than the average MAR crust, but at depths greater than 3 km velocities are comparable to average MAR values.

4.1. Subsurface Geometry of a Young Oceanic Detachment Fault

[15] Seafloor observations indicate that the TAG hydrothermal field is positioned on the hanging

Table 1. Summary of Traveltime Residual Statistics

Profile	Number of Picks	χ^2	RMS, ms	Model
1	1603	84.76	230	OH-1
		48.96	175	1-D
		1.82	49	2-D
2	344	55.89	187	OH-1
		24.83	124	1-D
		3.03	37	2-D
3	709	17.96	106	OH-1
		13.42	92	1-D
		0.98	33	2-D

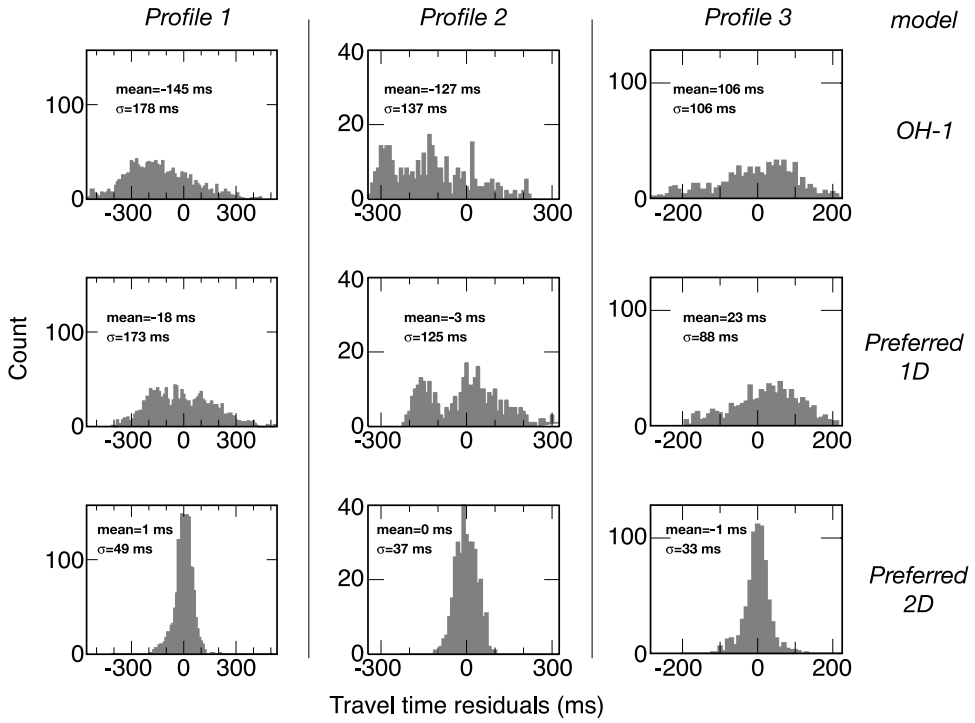

Figure 5. Histograms of traveltime residuals for Profiles 1, 2, and 3 (left to right), predicted by models OH-1 (Figure 4), best 1-D (Figure 4), and preferred 2-D (Figure 6) (top to bottom).

wall of a west-facing normal fault, ~2.5 km from the fault termination [e.g., *Kleinrock and Humphris*, 1996]. Magnetic data indicates that this extensional fault has been active for ~0.35 Myr [*Tivey et al.*, 2003], during which time deep crustal rocks (gabbros) have been uplifted and exposed on the seafloor [*Karson and Rona*, 1990; *Zonenshain et al.*, 1989]. It seems, however, that the fault has not been active long enough to expose mantle rocks, nor to form the typical corrugated dome that characterize many oceanic core complexes associated with mature detachment faults [*Cannat et al.*, 2006; *Escartín et al.*, 2003; *Tucholke et al.*, 1998]. The deep geometry of the fault has been recently inferred from a microearthquake study, which indicates that seismic activity along the fault is concentrated in a steeply dipping (~70°), ~12 km-long curved band at 3.0–6.5 km depth [*deMartin et al.*, 2007]. Thus the extant geological and geophysical data suggest that the TAG segment represents the early stages of development of a young oceanic detachment fault.

[16] Our results are consistent with a detachment-faulting model for extension at TAG, and provide new constraints on the shallow (<4 km depth) geometry of the fault system. The roughly triangular shape of the high-velocity zone along Profile 1 coincides spatially with the distribution of microseismicity along the rift valley floor [*deMartin et al.*, 2007] (Figure 8b), as well as the along-axis extent of the reduced magnetization zone [*Tivey et al.*, 2003]. These spatial correlations lead us to interpret the high-velocity body along the center of Profile 1 as the footwall of the detachment fault (Figures 6 and 8). In cross-axis view, our results show that lower crustal rocks with seismic velocities greater than 6.5 km s^{-1} occur at shallow depth at the eastern valley wall. This implies an uplift-along-detachment process that explains the contrasting seismic structure between Profiles 1 and 3, and creates a dipping interface between high-velocity footwall rocks and lower-velocity hanging wall rocks in across-axis Profile 2. The boundary between the high- and low-velocity regions of Figures 6 and 8 thus represents the detachment surface and fault plane in the upper section of the crust.

[17] From our across-axis model (Figures 6 and 8) we infer a fault dip of ~20 ± 5° within the upper 2 km, a section of the fault that seems to be aseismic [*deMartin et al.*, 2007]. This angle is similar to the angle of the fault scarp exposed on the seafloor [*Zonenshain et al.*, 1989], and it is consistent with the idea that oceanic detachment faults exhume the

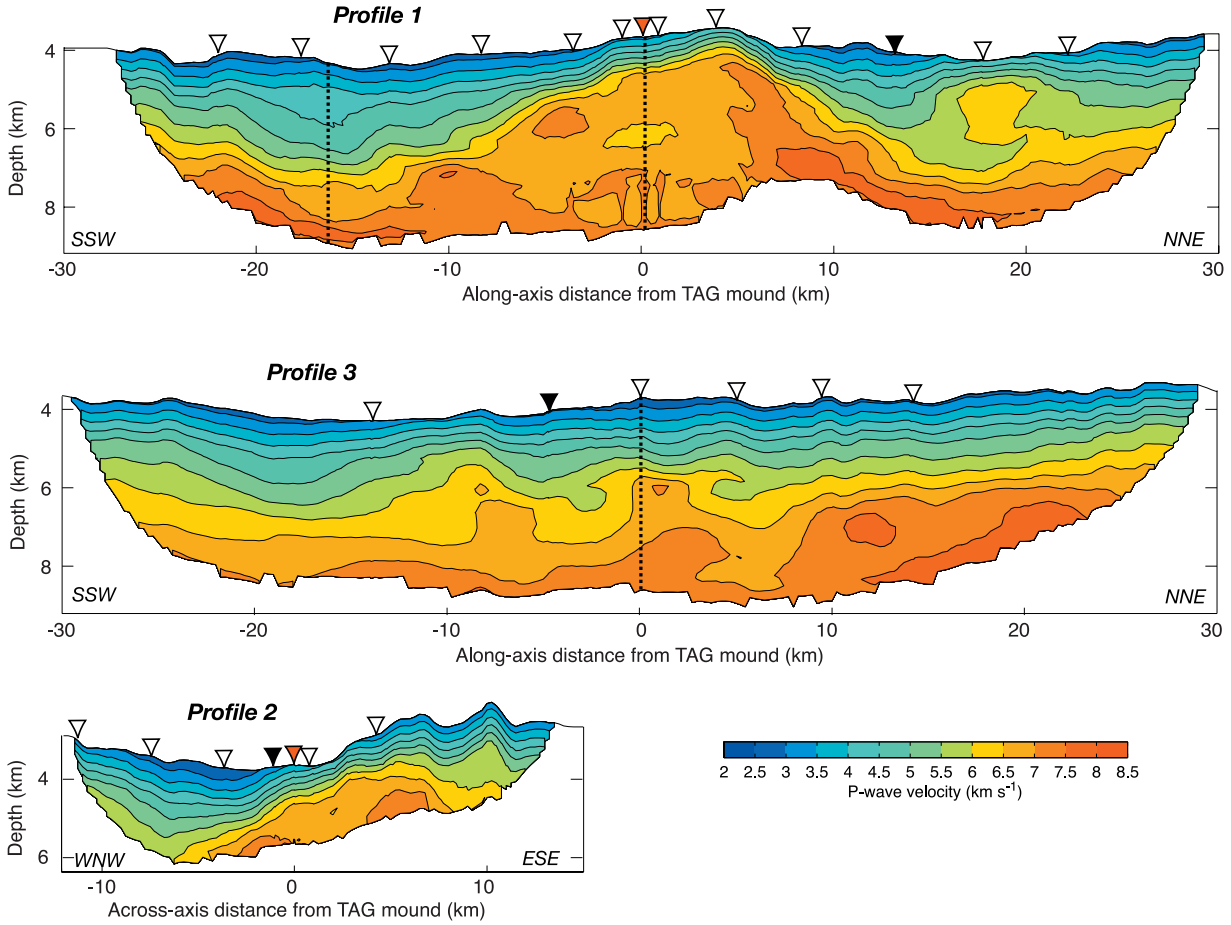

Figure 6. Preferred 2-D velocity models with contours every 0.5 km s^{-1}. Triangles are OBS positions on each cross section with black triangles corresponding to the instruments whose data are shown in Figure 2. Red triangle indicates the location of the TAG hydrothermal mound. Dashed vertical lines indicate the location of the velocity-depth profiles shown in Figure 7.

footwalls at low angles [*Dick et al.*, 1981; *Tucholke and Lin*, 1994]. However, it is much smaller than the ~70° angle delineated by the microseismicity within the 3–6.5 km depth range [*deMartin et al.*, 2007]. This implies that the detachment fault nucleates at high angles in a weak, deep zone, and that the footwall of the fault rolls over as it is exhumed, with the rotation occurring primarily at 2–3 km depth. This interpretation is consistent with models of flexural rotation of normal faults from high to low angle that have been proposed for both continental and oceanic settings [e.g., *Buck*, 1988; *Lavier et al.*, 1999]. Numerical models of lithospheric extension such as those of *Lavier et al.* [1999] and *Buck et al.* [2005] predict that fault rotation occurs at lateral scales of less than 5 km, comparable to the 1–2 km lateral scale inferred from our observations. In those numerical models, flexural rotation of the fault occurs along its exposed, inactive section. In contrast, our results indicate that rotation can occur at ~2–3 km depth, probably the depth at which flexural stresses exceed those of the brittle, low-cohesion uppermost crust of the hanging wall.

[18] Our results also provide constraints on the along-strike extent and geometry of the detachment fault. From our tomographic images we infer that the fault dips along-strike at shallow angles (~16° and ~8° to the north and south, respectively; Figure 8). This observation has implications for other detachment faults and oceanic core complexes. In oceanic core complexes that are not bounded by segment discontinuities, like the northern end of Atlantis massif, the along-strike termination of the exposed fault is not well understood. At Atlantis massif, the smooth corrugated detachment ends abruptly to the north where the seafloor fabric becomes more typical of abyssal hills and volcanic terrain [*Cann et al.*, 1997]. However, the fault appears to continue along strike beneath this

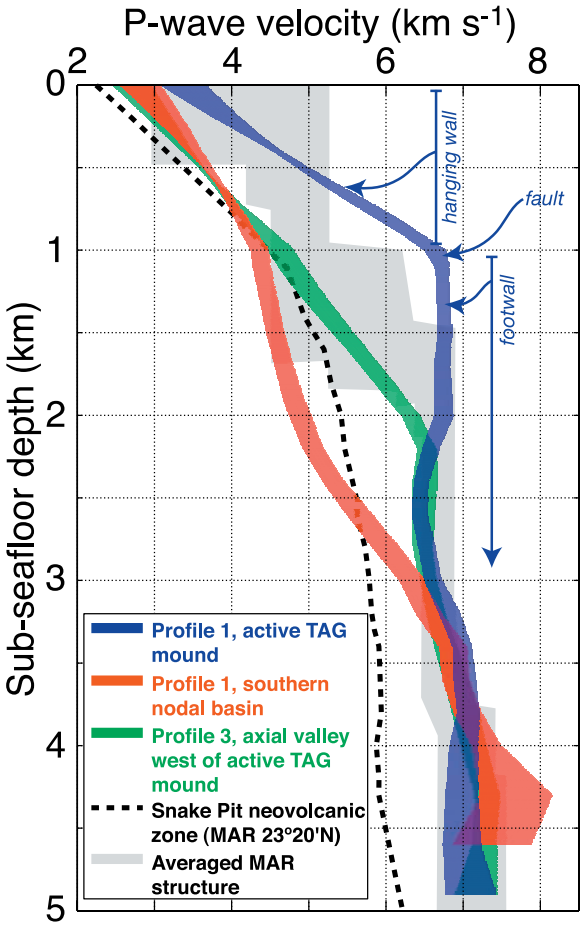

Figure 7. Velocity-depth profiles from TAG compared to profiles from the Snake Pit neovolcanic zone (MAR 23°20′N) and average young Atlantic crust [*White et al.*, 1992]. The velocity-depth profiles represent averages within 5-km-wide sections of each seismic profile; the width of the profiles corresponds to twice the estimated uncertainty of the velocity models at those locations (see Appendix A).

volcanic carapace, as inferred from seismic reflection data [*Canales et al.*, 2004]. *Reston and Ranero* [2005] suggest that the along-strike extent of detachment faults formed at slow spreading centers is larger than what can be inferred from the seafloor morphology. These authors argue that a significant part of a detachment fault may be buried by other small fault blocks transferred from the hanging wall to the footwall if the depth at which the fault becomes inactive varies along the spreading segment. The distribution of microseismicity that defines the deep geometry of the detachment fault, together with the seismic structure presented here, indicate that the detachment fault is a complex surface that dips both along the extension direction (with dip angle varying with depth) as well as along strike (Figure 8). The complex fault surface resembles a dome, rather than a simpler planar surface. The three-dimensional, subseafloor fault surface that we infer from our velocity models and the distribution of deep micro-earthquakes [*deMartin et al.*, 2007] (Figure 8b) is thus remarkably similar to the young, dome-shaped core complexes recently found in other regions of the MAR [*Smith et al.*, 2006]. It is this complex geometry that gives rise to a curved plate boundary [*deMartin et al.*, 2007] and the apparent truncation along-strike of the exposed footwall.

4.2. Thermal Structure of the Detachment Fault Footwall

[19] Our seismic velocity models, together with the extant geophysical information, also provide constraints on the thermal structure and composition of the detachment footwall beneath the TAG mound. Determining the thermal structure of the lithosphere within the axial rift valley is not trivial matter, since the distribution and longevity of heat sources, heat sinks, and faults during the past several hundred thousands of years is unknown. However, a good approximation can be obtained from two-dimensional numerical models of mid-ocean ridge faulting the accurately predict the formation of long-lived normal faults in the presence of an appropriate balance between dike intrusions and amagmatic extension [*Buck et al.*, 2005]. Figure 9a shows temperature-depth profiles at a distance of 3.8 km from the ridge axis obtained from thermomechanical modeling of detachment faulting considering a half spreading rate of 15 mm yr^{-1} [*Williams et al.*, 2006], following the method described by *Tucholke et al.* [2006]. Although these models do not include the effects on temperature of asthenospheric mantle upwelling, melting, and magma migration, they do account for the heat provided by dike injections at the ridge axis, as well as heat extraction by hydrothermal cooling, and accurately predict the style of deformation and faulting observed in the TAG area.

[20] In these models, hydrothermal cooling is simulated by enhancing the thermal conductivity of the regions with temperatures below 600°C and above 7 km depth by a factor *Nu* (Nusselt number) [*Phipps Morgan et al.*, 1987]. We constrain the range of plausible thermal models by choosing those that are consistent with the observed microseismicity beneath the TAG mound, which extends to ~5–6 km depth (Figure 9b) [*deMartin et al.*, 2007] and can be taken as the depth to the brittle-

plastic transition (BPT). For the case of $Nu = 2$, the geotherm intersects the BPT [*Hirth et al.*, 1998] at 4 km depth, while for $Nu = 4$ the geotherm intersect the BPT below 6 km depth (Figure 9a). Thus the thermal structure beneath the TAG mound is probably well approximated by these two end-member thermal models.

[21] We use laboratory-derived relationships between pressure, temperature, and compressional-wave velocity to test whether these geotherms are consistent with our seismic data. The velocity structure of the footwall beneath the TAG mound, which begins at ~1 km depth along Profile 1 (Figure 7), is characterized by P wave velocities

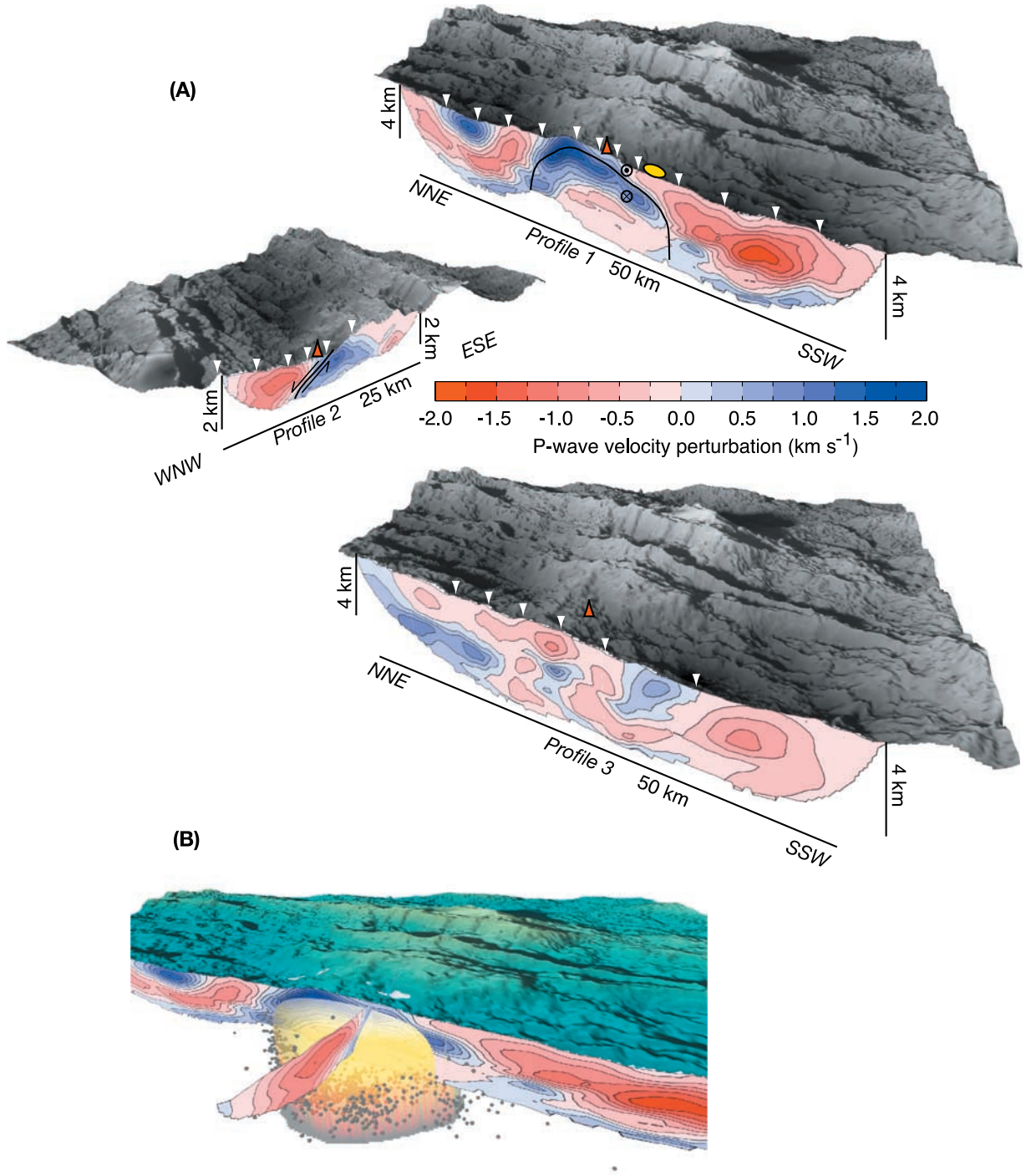

Figure 8

in the range of 6.5–7.0 km s^{-1} (Figures 7 and 9c). These velocities suggest that the footwall is composed primarily of gabbroic rocks and/or partially serpentinized peridotite [e.g., *Miller and Christensen*, 1997]. *deMartin et al.* [2007] estimate that the average V_P/V_S ratio of the TAG segment is ~2.0, which is consistent with laboratory measurements on serpentinized peridotites [*Miller and Christensen*, 1997]. However, their estimate is an average for the whole segment, not just the footwall, and it could reflect the highly tectonized nature of the hanging wall. Thus, for simplicity, we assume a purely gabbroic composition, consistent with submersible observations of gabbro exposures on fault scarps along the eastern valley wall [*Zonenshain et al.*, 1989], but the following interpretation is also valid for a more heterogeneous footwall composed of mafic and ultramafic rocks [e.g., *Cannat*, 1993]. We first compute the expected increase in V_P with increasing pressure. We find the pressure (P) derivative of V_P by fitting an equation of the form $V_P(P) = V_0 + b\ln(P)$ to laboratory measurements of V_P as a function of confining pressure (up to 200 MPa) on MAR gabbro samples [*Miller and Christensen*, 1997], assuming an effective pressure gradient of 25 MPa km^{-1} [*Carlson and Miller*, 2004]. We then calculate the effect of temperature on V_P using the temperature derivative of V_P reported by *Christensen* [1979] for gabbros. Finally, to make the predicted velocity-depth profiles directly comparable to our observations, we adjust the calculated V_P by 0.155 km s^{-1} so it matches our observations at 1.2 km depth.

[22] The predicted seismic velocities (Figure 9c) exceed our observations over the depth range from 1.2 km to ~3.0–3.5 km. Since we have already accounted for the effect of temperature on V_P, the mismatch can only be explained by the presence of melt or by fracturing and alteration. We rule out the former explanation because the predicted temperature within that depth range is significantly lower than the temperature of the gabbro solidus (Figure 9a), and because the BPT inferred from the seismicity is at least 5 km deep. Thus the most likely explanation for the mismatch is increased porosity within the upper part of the footwall. For example, a porosity of 0.003 in the form of water-filled cracks (aspect ratio of 0.01 [*Kuster and Töksoz*, 1974]) from 2 km to 2.4 km depth is sufficient to reduce the predicted seismic velocities to match our observations (Figure 9c). As discussed in section 4.1, the geometry of detachment fault delineated by the microseismicity and the tomography models indicates that the footwall suffers considerable rotation at 2–3 km depth as it is exhumed [*deMartin et al.*, 2007]. Such rotation is likely to damage the footwall, creating a section of increased porosity and fracturing within the footwall that can be exploited by fluids to contribute its cooling. Fluid flow within the fractured footwall can also alter the mineralogy, further contributing to the reduced seismic velocities. In the next section we investigate whether the heat mined from the footwall is sufficient to drive high-temperature hydrothermal convection beneath TAG.

4.3. Heat Source of the TAG Hydrothermal System

[23] A previous seismic study of the TAG segment [*Kong et al.*, 1992] reported the presence of a low-velocity zone at a depth of ~3–6 km, south of the active TAG mound at approximately 26°06′N, which was interpreted as a crustal magma body. Subsequent studies have assumed that this magma body is the primary heat source for hydrothermal convection at the TAG field. Our results, however, do not support these ideas as we do not find evidence for seismic low-velocity zones associated with crustal magma chambers or interstitial partial melt beneath the TAG mound. Nowhere along our profiles do we find a structure comparable to the anomalously low seismic velocities found beneath

Figure 8. (a) Three-dimensional perspective views of illuminated bathymetry and 2-D velocity perturbation models of the TAG segment. Triangles indicate the location of OBS. Red triangle also indicates the location of the TAG mound. Yellow ellipse in Profile 1 denotes the location of the volcanic feature referred to by *Kong et al.* [1992]. Our interpretation of the subsurface geometry of the detachment fault along Profiles 1 and 2 is shown by a thick solid line, which approximates the intersection between the fault plane and the 2-D crustal sections. Along Profile 1 the curved fault plane encloses the footwall, characterized by high velocities and with relative movement along the fault into the page. The hanging wall corresponds to the area above the fault plane, with relative movement out of the page. Along Profile 2, high velocities to the right of the fault plane correspond to the footwall, while the hanging wall is to the left of the fault. Arrows indicate relative movement along the fault. (b) Three-dimensional oblique view of illuminated bathymetry of the TAG segment and velocity perturbation models for Profiles 1 and 2 (color scale as in Figure 8a). The semitransparent yellow surface is an approximate three-dimensional rendition of a fault surface that is consistent with the high-velocity anomalies found along the seismic profiles, as well as with the local microseismicity (gray dots) [*deMartin et al.*, 2007].

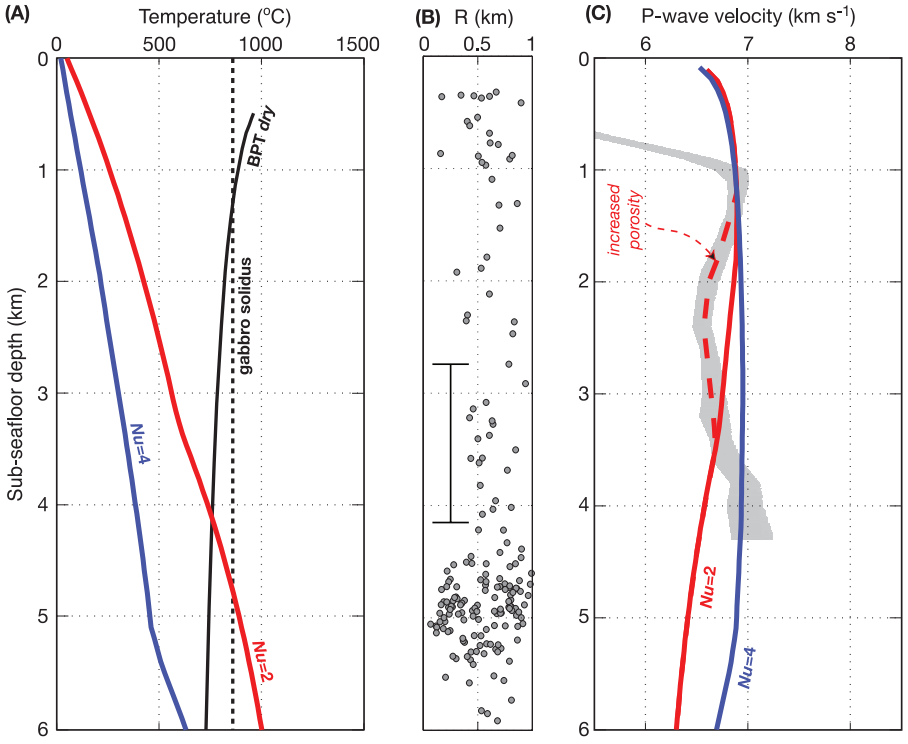

Figure 9. (a) Temperature-depth profiles at a distance of 3.8 km from the ridge axis predicted by thermomechanical modeling for a half spreading rate of 15 mm yr^{-1} [*Williams et al.*, 2006]. Models were computed for Nusselt numbers (*Nu*) of 2 (red line) and 4 (blue line) (see text for definition of *Nu*), and assuming that half of the plate separation is accommodated by dike intrusions (M = 0.5 [*Buck et al.*, 2005]). More details on the model assumptions and parameters used are given by *Tucholke et al.* [2006]. Also shown are the solidus temperature for gabbro [*Coogan et al.*, 2001] (dashed line) and the temperature-depth profile of the brittle-plastic transition (BPT) for dry crustal rheology [*Hirth et al.*, 1998] (solid black line). (b) Microseismicity beneath the active TAG mound observed from June 2003 to March 2004 (data from the catalog of *deMartin et al.* [2007]). Only events with an epicentral distance R of less than 1 km from the active TAG mound are shown. Vertical bar shows the estimated depth uncertainty of the events [*deMartin et al.*, 2007]. Note the sharp decrease in seismicity below ~5 km depth. (c) Predicted velocity-depth profiles for a gabbroic footwall using geotherms shown in Figure 9a (solid red and blue lines for Nu = 2 and 4, respectively). Also shown in gray is the velocity-depth profile found beneath the TAG mound along Profile 1 for the solution shown in Appendix A (Figure A4). Red dashed line shows the estimated reduction in V_P assuming an increased porosity of 0.003 from 2 to 2.4 km depth (for the case of Nu = 2). Porosity effects on compressional velocity have been calculated using the theoretical formulations of seismic propagation in two-phase media of *Kuster and Töksoz* [1974], assuming a shear and bulk modulus of the gabbroic matrix of 43 and 80 GPa, respectively [*Miller and Christensen*, 1997], shear and bulk modulus of the inclusions of 0 and 2.3 GPa [*Kuster and Töksoz*, 1974], respectively, densities of 2900 and 1030 kg m^{-3} for the matrix and inclusions, respectively, and an aspect ratio for the inclusions of 0.01 to simulate cracks.

the Snake Pit neovolcanic zone in the MARK area (Figure 7), where there are clear indications of crustal melt [*Canales et al.*, 2000]. The only place in our study area where seismic velocities are anomalously low compared to average MAR values is the basin at the southern end of the segment, where velocities as low as 5 km s^{-1} are found at 2 km depth. However, at this site the seismic structure below 3 km depth resembles the average Atlantic structure, indicating that the low upper crustal seismic velocities at this location result from increased porosity in the basin, possibly due to fracturing and subsequent infilling by extrusive lavas, in agreement with similar patterns found at other segment ends along the MAR [e.g., *Hooft et al.*, 2000].

[24] Resolution tests indicate that our experiment could detect low-velocity zones beneath the TAG mound if they are shallower than 4 km and extend at least 3 km in the along-axis direction (see Appendix A). This means that we should have imaged a feature like the low-velocity zone of *Kong et al.* [1992] if it was real. The low-velocity zone of *Kong et al.* [1992] was present in inversions that utilized traveltime residuals from both

controlled sources and microearthquakes, but not in inversions that used controlled-source data alone [*Kong*, 1990]. The joint inversion including microearthquake data with the resulting low-velocity zone was preferred over the refraction-only inversion because of attenuation observed in seismic arrivals from shots to the south of the active TAG mound. We also observed some attenuation in this region (southern parts of Profiles 1 and 3; Figure 2), but we interpret it as resulting from low-velocity, high-porosity upper crust in the southern nodal basin. Although there are differences in experimental geometry and data acquisition parameters between our study and *Kong et al.*'s [1992] study (e.g., 166 shots recorded in 13 receivers along our Profile 1 compared to 23 shots and 31 earthquakes recorded in 7 receivers in *Kong et al.*'s [1992] final model), they do not fully explain the differences in velocity models, especially considering that *Kong*'s [1990] refraction-only inversion yielded very similar results to our Profile 1 inversion. We thus believe that the low-velocity zone presented by *Kong et al.* [1992] was an artifact due to the use of microearthquakes in a joint tomographic inversion, which can arise from irresolvable trade-offs between hypocentral depth and seismic velocity.

[25] *Cannat et al.* [2004] point out that heat advected by tectonic uplift might contribute to the thermal structure of young oceanic lithosphere. Although early models of hydrothermal fluid flow along fault zones concluded that conductive heat transfer across a fault is insufficient to drive a high-temperature hydrothermal system [*Cann and Strens*, 1982; *Strens and Cann*, 1982], those models considered only small normal faults that penetrated the upper 500–1000 m of the crust, and not large, long-lived faults such as the detachment beneath the active TAG mound. Therefore, in the absence of crustal magma reservoirs in the vicinity of the TAG mound, the presence of a large (>10 km along axis) detachment fault, and indications of water-filled cracks in the upper part of the footwall from our tomography results, it seems plausible that part of the energy driving hydrothermal circulation at TAG results from (1) conductive heat extracted by fluids penetrating the fractured upper part of the footwall and/or (2) heat advected by uplift along the fault and transferred conductively across the fault surface.

[26] To estimate the energy flux per unit area available to the TAG hydrothermal system due to conductive and hydrothermal cooling of the footwall we use Fourier's law $Q_c = Nu\ k\frac{dT}{dz}$ relating the heat flux per unit area Q_c to the thermal gradient $\frac{dT}{dz}$ across the footwall, with a thermal conductivity k enhanced by a factor of Nu. For values of Nu between 2 and 4, $\frac{dT}{dz}$ in the upper 3 km of the crust ranges from ~290 to ~500 K km^{-1}, respectively (Figure 9a), resulting in an average Q_c of 1.0 W m^{-2} (for k = 2.604 W m^{-1} K^{-1} [*Cannat et al.*, 1995]). To evaluate the contribution of the second mechanism, we estimate the heat flux per unit area Q_a advected by uplift along the fault and extracted by fluids circulating in hot rock, expressed in terms of the uplift rate u as $Q_a = u\rho C_p \Delta T$ [e.g., *Lister*, 1974], where ρ is the density of the host rock (2900 kg m^{-3}), C_p is the specific heat (1200 J kg^{-1} K^{-1} [*Cannat et al.*, 2004]), and ΔT is the temperature contrast between the hot rock and the fluid (600 K). The uplift rate, assuming a 60° average fault dip and a horizontal extension of 3.9 km during 0.35 Myr [*Tivey et al.*, 2003], is 19 km Myr^{-1}. Thus Q_a is 1.3 W m^{-2}.

[27] Therefore the heat flux per unit area available to the system by advection and conduction is $Q = Q_c + Q_a$ = 2.3 W m^{-2}. This means that if the total heat flux of the TAG system (Q_T = 1000 MW [*Humphris and Cann*, 2000]) comes from conduction and tectonically advected heat, the area from which fluids are mining energy has to be ~430 km^2, significantly larger than the ~100 km^2 covered by the detachment fault. Thus these mechanisms might contribute no more than ~25% to the total heat required to drive the TAG system.

[28] These calculations show that a large, and/or frequently replenished melt reservoir is required to provide enough heat to drive high-temperature convection at TAG. The magmatic heat source must be deeper than 4 km to satisfy our seismic refraction data, and it must also be deeper than ~7 km to be consistent with the observation of deep seismicity [*deMartin et al.*, 2007]. In this regard, detachment faulting at TAG may be similar to melt-assisted detachments like the Atlantis Bank on the Southwest Indian Ridge [*Dick et al.*, 2000]. A deep magmatic heat source of this kind may also serve as a nucleation point and root zone for detachment faulting.

5. Concluding Remarks

[29] In summary, the seismic structure of the TAG segment presented in this paper shows that the TAG hydrothermal system is not driven by energy

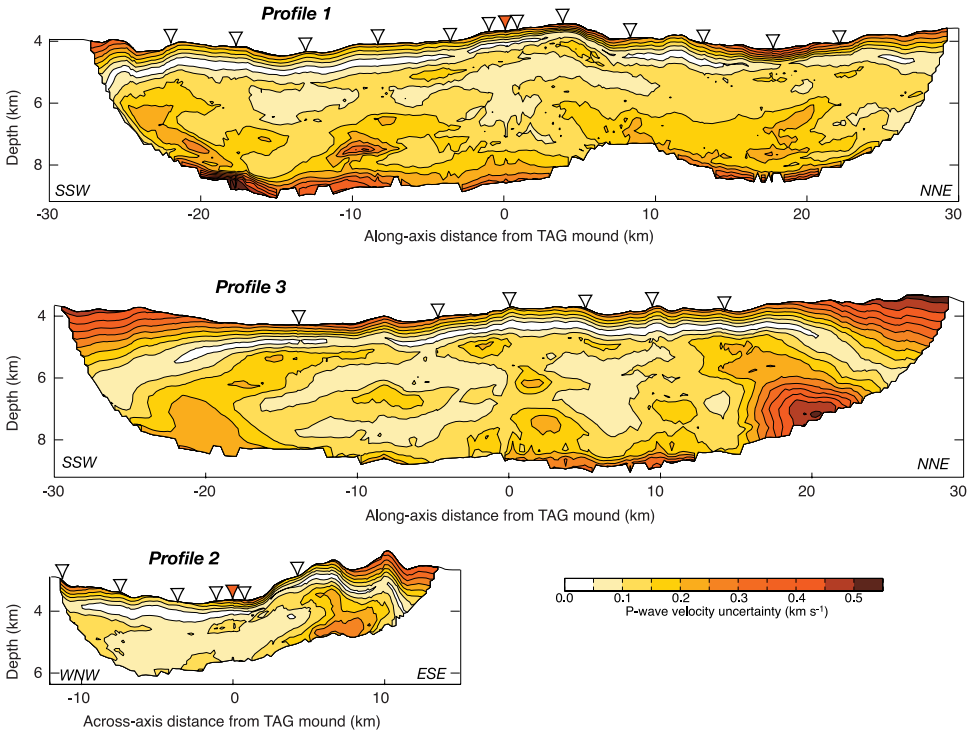

Figure A1. *P* wave velocity uncertainty along each profile. Triangles are OBS. Red triangle also indicates the location of the TAG hydrothermal mound.

extracted from shallow or mid-crustal magmatic intrusions. Our results, together with recent microseismicity observations, (1) reveal the complex, dome-shaped subsurface geometry of a detachment fault, (2) suggest that significant rotation of the footwall fractures the upper part of the footwall, contributing to its cooling, and (3) indicate that the most likely heat source of the active TAG mound must be magmatic intrusions at the spreading axis at least 7 km deep. Uplift along the fault cannot provide enough heat to drive hydrothermal circulation in this system, but it can promote efficient fluid up-flow, channeling deep hydrothermal fluids from a large area along the segment (~20 km, the length of the active fault) to a focused area near the surface where they are expelled to the seafloor through a high-porosity zone in the hanging wall

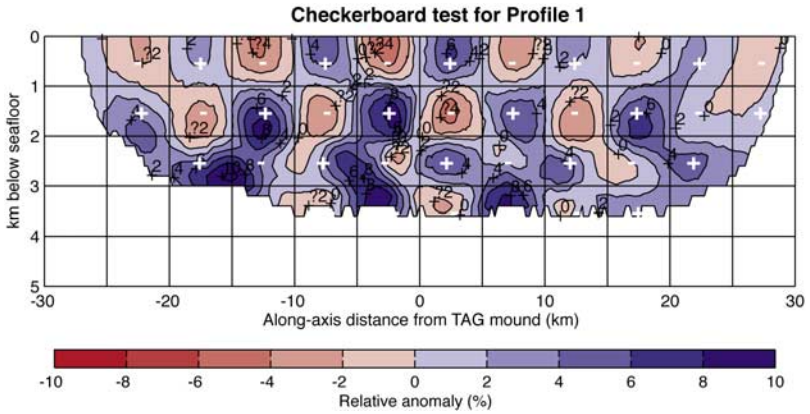

Figure A2. Results from a checkerboard resolution test.

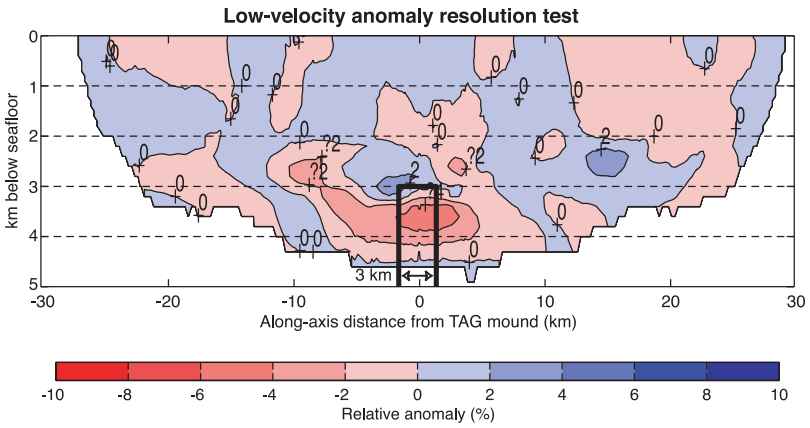

Figure A3. Results from a low-velocity anomaly resolution test. Rectangle delineates the location of the initial anomaly, which had a reduction in V_P of 10% with respect to a background 1-D structure.

where fractures are kept open by episodic slip along the fault.

Appendix A: Model Uncertainty and Resolution Tests

[30] To estimate the uncertainty of our velocity models we followed a Monte Carlo approach [e.g., *Korenaga et al.*, 2000]. First we constructed 10 traveltime data sets by adding random Gaussian noise $N(0, \sigma = 15$ ms km$^{-1})$ to the observed traveltime gradients, following the method of *Zhang and Toksöz* [1998]. We then constructed 10 initial velocity models by adding random perturbations to the best 1-D models (the perturbations were constrained to be within -1 km s^{-1} and +0.2 km s^{-1} with respect to the 1-D model). Finally we run 100 tomographic inversions using all possible combinations of perturbed traveltimes and perturbed initial velocity models, and using the same model parameterization as in our preferred solutions. Assuming that all the Monte Carlo realizations have the same probability, the estimated velocity uncertainty can be approximated by the standard deviation of the 100 Monte Carlo realizations (Figure A1).

[31] We tested the spatial resolution of our preferred 2-D models by performing a checkerboard test for Profile 1. First we added sinusoidal velocity perturbations of ±10% to the 1-D velocity models in 5 × 1 km^2 cells, alternating positive and negative perturbations, and calculated the predicted traveltimes by the perturbed velocity model. Then we added noise to the predicted traveltimes using the method described above, and performed a tomographic inversion using the same model parameterization as in our preferred solution. The recovered checkerboard pattern (Figure A2) shows that our experiment is able to resolve features with length scales of 5 km horizontally and 1 km vertically, assuming velocity variations of ±10%.

[32] Checkerboard tests provide an upper bound of the average resolution of the full models. However, the resolution of the models can be higher for isolated anomalies in a relatively homogenous medium. To test if our experiment could detect low-velocity zones beneath the TAG mound, we reduced the velocity of the 1-D model along Profile 1 by 10% in a 3-km wide area centered at the TAG mound at depths below 3 km (black box in Figure A3). We then calculated the predicted traveltimes, added random noise as described above, and inverted for the 2-D structure. The recovered anomaly (Figure A3) is smeared laterally but is nevertheless clearly visible, demonstrating that our tomographic inversions are capable of resolving low-velocity anomalies beneath the TAG mound if they are at least 3 km long and shallower than 4 km.

[33] We also tested the significance of the small decrease in P wave velocity found along Profile 1 beneath the TAG mound at depths of ~2–3 km (Figure 7). We modified the preferred 2-D model of Profile 1 (Figure 6) so that the velocity gradient in the area within 6 km from the TAG mound remains positive with depth (Figure A4). We use this modified 2-D model as starting model and run the tomographic inversion of the observed data with the same smoothing model parameterization as in our preferred solution. The resulting velocity

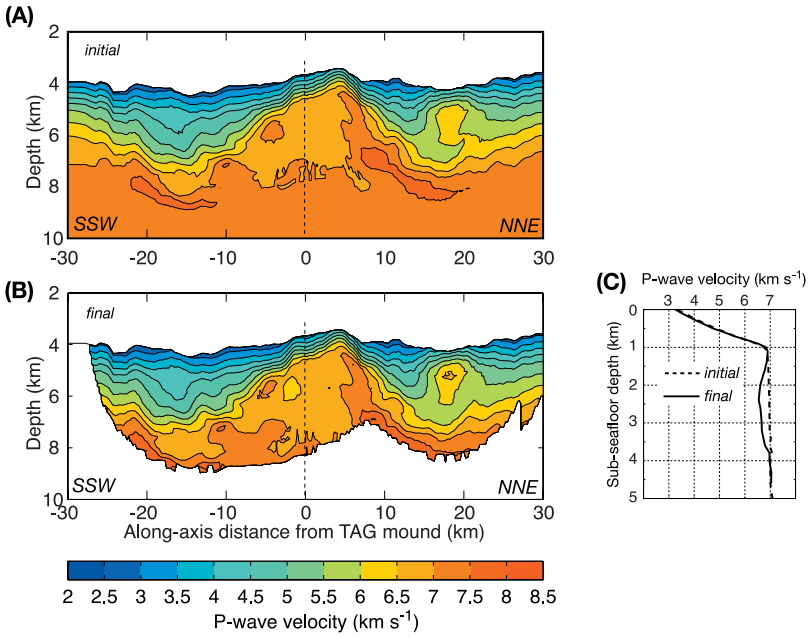

Figure A4. Resolution test for a negative velocity gradient in the vicinity of the TAG mound. (a) Initial model. (b) Final model. Dashed vertical lines show location of the profiles shown in Figure A4c. (c) Velocity-depth profiles extracted at X = 0 for the initial (dashed) and final (solid) models.

model shows a negative velocity gradient from 1 to 2.5 (Figure A4). The decrease in velocity is less pronounced that in our preferred solution (Figure 7), but it starts shallower. Thus the negative velocity gradient beneath the TAG mound is required by the data, although there is a trade-off between the amplitude of the velocity decrease and the thickness of the anomalous zone.

Acknowledgments

[34] We thank the captains, crew, and participants of the three cruises involved in this experiment: R/V *Atlantis* Voyage 7-36, R/V *Maurice Ewing* Cruise 03-09, and R/V *Knorr* Voyage 76 Leg IV. We also thank the personnel of the US OBSIP groups at Lamont-Doherty Earth Observatory and Woods Hole Oceanographic Institution, whose skills and dedication contributed to this excellent seismic data set. We are thankful to M. Behn, J. Cann, J. Escartín, and G. Hirth for fruitful discussions and comments on various aspects of this study and to M. Behn and C. Williams for kindly providing us the thermal models shown in Figure 9. The original manuscript benefited from constructive criticism by reviewer D. Blackman and Editor P. van Keken. This research was supported by NSF grant OCE-0137329.

References

Buck, W. R. (1988), Flexural rotation of normal faults, *Tectonics*, *7*, 959–973.

Buck, W. R., L. L. Lavier, and A. N. B. Poliakov (2005), Modes of faulting at mid-ocean ridges, *Nature*, *434*, 719–723.

Canales, J. P., J. A. Collins, J. Escartín, and R. S. Detrick (2000), Seismic structure across the rift valley of the Mid-Atlantic Ridge at 23°20′N (MARK area): Implications for crustal accretion processes at slow spreading ridges, *J. Geophys. Res.*, *105*, 28,411–28,425.

Canales, J. P., B. E. Tucholke, and J. A. Collins (2004), Seismic reflection imaging of an oceanic detachment fault: Atlantis megamullion (Mid-Atlantic Ridge, 30°10′N), *Earth Planet. Sci. Lett.*, *222*, 543–560.

Canales, J. P., S. C. Singh, R. S. Detrick, S. M. Carbotte, A. J. Harding, G. M. Kent, J. B. Diebold, J. Babcock, and M. R. Nedimovic (2006), Seismic evidence for variations in axial magma chamber properties along the southern Juan de Fuca Ridge, *Earth Planet. Sci. Lett.*, *246*, 353–366.

Cann, J. R., and M. R. Strens (1982), Black smokers fuelled by freezing magma, *Nature*, *298*, 147–149.

Cann, J. R., M. R. Strens, and A. Rice (1985), A simple magma-driven thermal balance model for the formation of volcanogenic massive sulphides, *Earth Planet. Sci. Lett.*, *76*, 123–134.

Cann, J. R., D. K. Blackman, D. K. Smith, E. McAllister, B. Janssen, S. Mello, E. Avgerinos, A. R. Pascoe, and J. Escartín (1997), Corrugated slip surfaces formed at ridge-transform intersections on the Mid-Atlantic Ridge, *Nature*, *385*, 329–332.

Cannat, M. (1993), Emplacement of mantle rocks in the seafloor at mid-ocean ridges, *J. Geophys. Res.*, *98*, 4163–4172.

Cannat, M., et al. (1995), *Proceedings of the Ocean Drilling Program, Initial Reports*, vol. 153, Ocean Drill. Program, College Station, Tex.

Cannat, M., J. R. Cann, and J. MacLennan (2004), Some hard rock constraints on the supply of heat to mid-ocean ridges, in *Mid-Ocean Ridges: Hydrothermal Interactions Between the Lithosphere and the Oceans*, *Geophys. Monogr. Ser.*, vol. 148, edited by C. R. German et al., pp. 111–149, AGU, Washington, D. C.

Cannat, M., V. Mendel, E. Ruellan, K. Okino, J. Escartín, V. Combier, and M. Baala (2006), Modes of seafloor generation at a melt-poor ultraslow-spreading ridge, *Geology*, *34*, 605–608.

Carlson, R. L., and D. J. Miller (2004), Influence of pressure and mineralogy on seismic velocities in oceanic gabbros: Implications for the composition and state of the lower oceanic crust, *J. Geophys. Res.*, *109*, B09205, doi:10.1029/2003JB002699.

Christensen, N. I. (1979), Compressional wave velocities in rocks at high temperatures and pressures, critical thermal gradients, and crustal low-velocity zones, *J. Geophys. Res.*, *84*, 6849–6857.

Coogan, L. A., R. N. Wilson, K. M. Gillis, and C. J. MacLeod (2001), Near-solidus evolution of oceanic gabbros: Insights from amphibole geochemistry, *Geochim. Cosmochim. Acta*, *65*, 4339–4357.

deMartin, B. J., R. A. Sohn, J. P. Canales, and S. E. Humprhis (2007), Kinematics and geometry of active detachment faulting beneath the Trans-Atlantic Geotraverse (TAG) hydrothermal field on the Mid-Atlantic Ridge, *Geology*, *35*, 711–714.

Detrick, R. S., P. Buhl, E. E. Vera, J. C. Mutter, J. A. Orcutt, J. A. Madsen, and T. M. Brocher (1987), Multi-channel seismic imaging of a crustal magma chamber along the East Pacific Rise, *Nature*, *326*, 35–41.

Dick, H. J. B., G. Thompson, and W. B. Bryan (1981), Low-angle faulting and steady-state emplacement of plutonic rocks at ridge-transform intersections, *Eos Trans. AGU*, *62*, 406.

Dick, H. J. B., et al. (2000), A long in situ section of the lower ocean crust: Results of ODP Leg 176 drilling at the Southwest Indian ridge, *Earth Planet. Sci. Lett.*, *179*, 31–51.

Dunn, R. A., D. R. Toomey, and S. C. Solomon (2000), Three-dimensional seismic structure and physical properties of the crust and shallow mantle beneath the East Pacific Rise at 9°30′N, *J. Geophys. Res.*, *105*, 23,537–23,555.

Escartín, J., C. Mével, C. J. MacLeod, and A. M. McCaig (2003), Constraints on deformation conditions and the origin of oceanic detachments: The Mid-Atlantic Ridge core complex at 15°45′N, *Geochem. Geophys. Geosyst.*, *4*(8), 1067, doi:10.1029/2002GC000472.

Hirth, G., J. Escartín, and J. Lin (1998), The rheology of the lower oceanic crust: Implications for lithospheric deformation at Mid-Ocean ridges, in *Faulting and Magmatism at Mid-Ocean Ridges*, *Geophys. Monogr. Ser.*, vol. 106, edited by W. R. Buck et al., pp. 291–303, AGU, Washington, D. C.

Hooft, E. E. E., R. S. Detrick, D. R. Toomey, J. A. Collins, and J. Lin (2000), Crustal and upper mantle structure along three contrasting spreading segments of the Mid-Atlantic Ridge, 33.5°–35°N, *J. Geophys. Res.*, *105*, 8205–8226.

Humphris, S. E., and J. R. Cann (2000), Constraints on the energy and chemical balances of the modern TAG and ancient Cyprus seafloor sulfide deposits, *J. Geophys. Res.*, *105*, 28,477–28,488.

Humphris, S. E., et al. (1995), The internal structure of an active sea-floor massive sulphide deposit, *Nature*, *377*, 713–716.

Karson, J. A., and P. A. Rona (1990), Block-tilting, transfer faults, and structural control of magmatic and hydrothermal processes in the TAG area, Mid-Atlantic Ridge 26°N, *Geol. Soc. Am. Bull.*, *102*, 1635–1645.

Kleinrock, M. C., and S. E. Humphris (1996), Structural asymmetry of the TAG rift valley: Evidence from a near-bottom survey for episodic spreading, *Geophys. Res. Lett.*, *23*, 3439–3442.

Kong, L. S. L. (1990), Variations in structure and tectonics along the Mid-Atlantic Ridge, 23°N and 26°N, Ph.D. thesis, 341 pp, Mass. Inst. of Technol./Woods Hole Oceanogr. Inst., Woods Hole, Mass.

Kong, L. S. L., S. C. Solomon, and G. M. Purdy (1992), Microearthquake characteristics of a mid-ocean ridge along-axis high, *J. Geophys. Res.*, *97*, 1659–1685.

Korenaga, J., W. S. Holbrook, G. M. Kent, P. B. Kelemen, R. S. Detrick, H.-C. Larsen, J. R. Hopper, and T. Dahl-Jensen (2000), Crustal structure of the southeast Greenland margin from joint refraction and reflection seismic tomography, *J. Geophys. Res.*, *105*, 21,591–21,614.

Kuster, G. T., and M. N. Töksoz (1974), Velocity and attenuation of seismic waves in two-phase media: Part I. Theoretical formulations, *Geophysics*, *39*, 587–606.

Lalou, C., J.-L. Reyss, E. Brichet, P. A. Rona, and G. Thompson (1995), Hydrothermal activity on a 105 year scale at a slow-spreading ridge, TAG hydrothermal field, Mid-Atlantic Ridge 26°N, *J. Geophys. Res.*, *100*, 17,855–17,862.

Lavier, L. L., W. R. Buck, and A. N. B. Poliakov (1999), Self-consistent rolling-hinge model for the evolution of large-offset low-angle normal faults, *Geology*, *27*, 1127–1130.

Lister, C. R. B. (1974), On the penetration of water into hot rock, *Geophys. J. R. Astron. Soc.*, *39*, 465–509.

Martinez, F., B. Taylor, E. T. Baker, J. A. Resing, and S. L. Walker (2006), Opposing trends in crustal thickness and spreading rate along the back-arc Eastern Lau Spreading Center: Implications for controls on ridge morphology, faulting, and hydrothermal activity, *Earth Planet. Sci. Lett.*, *245*, 655–672.

Miller, D. J., and N. I. Christensen (1997), Seismic velocities of lower crustal and upper mantle rocks from the slow spreading Mid-Atlantic Ridge, south of the Kane transform zone (MARK), *Proc. Ocean Drill. Program Sci. Results*, *153*, 437–454.

Phipps Morgan, J., E. M. Parmentier, and J. Lin (1987), Mechanisms for the origin of mid-ocean ridge axial topography: Implications for the thermal and mechanical structure of accreting plate boundaries, *J. Geophys. Res.*, *92*, 12,823–12,836.

Reston, T. J., and C. R. Ranero (2005), Detachment faulting within slow-spreading segments—Beyond the corrugated surface, *Eos Trans. AGU*, *86*(52), Fall Meet. Suppl., Abstract T34B-05.

Rona, P. A., G. Klinkhammer, T. A. Nelsen, J. H. Trefry, and H. Elderfield (1986), Black smokers, massive sulphides and vent biota at the Mid-Atlantic Ridge, *Nature*, *321*, 33–37.

Singh, S. C., G. M. Kent, J. S. Collier, A. J. Harding, and J. A. Orcutt (1998), Melt to mush variations in crustal magma properties along the ridge crest at the southern East Pacific Rise, *Nature*, *394*, 874–878.

Singh, S. C., W. C. Crawford, H. Carton, T. Seher, V. Combier, M. Cannat, J. P. Canales, D. Dusunur, J. Escartín, and M. J. Miranda (2006), Discovery of a magma chamber and faults beneath a Mid-Atlantic Ridge hydrothermal field, *Nature*, *442*, 1029–1032.

Smith, D. K., J. R. Cann, and J. Escartín (2006), Widespread active detachment faulting and core complex formation near 13°N on the Mid-Atlantic Ridge, *Nature*, *442*, doi:10.1038/nature04950.

Strens, M. R., and J. R. Cann (1982), A model of hydrothermal circulation in fault zones at mid-ocean ridges, *Geophys. J. R. Astron. Soc.*, *71*, 225–240.

Tivey, M. A., H. Schouten, and M. C. Kleinrock (2003), A near-bottom magnetic survey of the Mid-Atlantic Ridge axis

at 26°N: Implications for the tectonic evolution of the TAG segment, *J. Geophys. Res.*, *108*(B5), 2277, doi:10.1029/2002JB001967.

Tucholke, B. E., and J. Lin (1994), A geological model for the structure of ridge segments in slow spreading ocean crust, *J. Geophys. Res.*, *99*, 11,937–11,958.

Tucholke, B. E., J. Lin, and M. C. Kleinrock (1998), Megamullions and mullion structure defining oceanic metamorphic core complexes on the Mid-Atlantic Ridge, *J. Geophys. Res.*, *103*, 9857–9866.

Tucholke, B. E., M. D. Behn, W. R. Buck, R. Qin, and J. Lin (2006), The role of melt supply in the formation of long-lived oceanic detachment faults, *Eos Trans. AGU*, *87*(52), Fall Meet. Suppl., Abstract V23-E0700.

Van Ark, E. M., R. S. Detrick, J. P. Canales, S. M. Carbotte, A. J. Harding, G. M. Kent, M. R. Nedimovic, W. S. D. Wilcock, J. B. Diebold, and J. M. Babcock (2007), Seismic structure of the Endeavour Segment, Juan de Fuca Ridge: Correlations with seismicity and hydrothermal activity, *J. Geophys. Res.*, *112*, B02401, doi:10.1029/2005JB004210.

White, R. S., D. McKenzie, and R. K. O'Nions (1992), Oceanic crustal thickness from seismic measurements and rare earth element inversions, *J. Geophys. Res.*, *97*, 19,683–19,715.

Wilcock, W. S. D., and J. R. Delaney (1996), Mid-ocean ridge sulfide deposits: Evidence for heat extraction from magma chambers or cracking fronts?, *Earth Planet. Sci. Lett.*, *145*, 49–64.

Williams, C. M., M. A. Tivey, and M. D. Behn (2006), The magnetic structure of Kane megamullion: Results from marine magnetic anomalies, paleomagnetic data and thermal modeling, *Eos Trans. AGU*, *87*(52), Fall Meet. Suppl., Abstract T42A-03.

Zelt, C. A., and D. A. Forsyth (1994), Modeling wide-angle seismic data for crustal structure: Southeastern Grenville Province, *J. Geophys. Res.*, *99*, 11,687–11,704.

Zhang, J., and M. N. Toksöz (1998), Nonlinear refraction traveltime tomography, *Geophysics*, *63*, 1726–1737.

Zonenshain, L. P., M. I. Kuzmin, A. P. Lisitsin, Y. A. Bogdanov, and B. V. Baranov (1989), Tectonics of the Mid-Atlantic rift valley between the TAG and MARK areas (26°–24°N): Evidence for vertical tectonism, *Tectonophysics*, *159*, 1–23.